
# Rapid Dimming Followed by a State Transition: A Study of the Highly Variable Nuclear Transient AT 2019avd over 1000+ Days

The Astrophysical Journal, 962:78 (15pp), 2024 February 10 https://doi.org/10.3847/1538-4357/ad182b


# Rapid Dimming Followed by a State Transition: A Study of the Highly Variable Nuclear Transient AT 2019avd over 1000+ Days

Yanan Wang[1,2], Dheeraj R. Pasham[3], Diego Altamirano[2], Andrés Gúrpide[2], Noel Castro Segura[2], Matthew Middleton[2], Long Ji[4], Santiago del Palacio[5], Muryel Guolo[6], Poshak Gandhi[2], Shuang-Nan Zhang[7,8], Ronald Remillard[3], Dacheng Lin[9], Megan Masterson[3], Ranieri D. Baldi[2,10], Francesco Tombesi[11,12,13,14], Jon M. Miller[15], Wenda Zhang[1], and Andrea Sanna[16]

[1] National Astronomical Observatories, Chinese Academy of Sciences, 20A Datun Road, Beijing 100101, People's Republic of China
[2] Physics & Astronomy, University of Southampton, Southampton, Hampshire, SO17 1BJ, UK
[3] Kavli Institute for Astrophysics and Space Research, Massachusetts Institute of Technology, Cambridge, MA 02139, USA
[4] School of Physics and Astronomy, Sun Yat-sen University, 2 Daxue Road, Zhuhai, Guangdong 519082, People's Republic of China
[5] Department of Space, Earth and Environment, Chalmers University of Technology, SE-412 96 Gothenburg, Sweden
[6] Department of Physics and Astronomy, Johns Hopkins University, 3400 N. Charles Street, Baltimore, MD 21218, USA
[7] Key Laboratory for Particle Astrophysics, Institute of High Energy Physics, Chinese Academy of Sciences, 19B Yuquan Road, Beijing 100049, People's Republic of China
[8] University of Chinese Academy of Sciences, Chinese Academy of Sciences, Beijing 100049, People's Republic of China
[9] Department of Physics, Northeastern University, Boston, MA 02115-5000, USA
[10] INAF—Istituto di Radioastronomia, Via P. Gobetti 101, I-40129 Bologna, Italy
[11] Dipartimento di Fisica, Univerisità di Roma Tor Vergata, via della Ricerca Scientifica 1, I-00133 Roma, Italy
[12] INAFOsservatorio Astronomico di Roma, Via Frascati 33, I-00040 Monte Porzio Catone, Italy
[13] Department of Astronomy, University of Maryland, College Park, MD 20742, USA
[14] NASA/Goddard Space Flight Center, Code 662, Greenbelt, MD 20771, USA
[15] Department of Astronomy, University of Michigan, 1085 South University Avenue, Ann Arbor, MI 48109, USA
[16] Dipartimento di Fisica, Università degli Studi di Cagliari, SP Monserrato-Sestu km 0.7, I-09042 Monserrato, Italy
*Received 2023 September 26; revised 2023 December 12; accepted 2023 December 20; published 2024 February 8*

## Abstract

The tidal disruption of a star around a supermassive black hole (SMBH) offers a unique opportunity to study accretion onto an SMBH on a human timescale. We present results from our 1000+ days monitoring campaign of AT 2019avd, a nuclear transient with tidal-disruption-event-like properties, with NICER, Swift, and Chandra. Our primary finding is that approximately 225 days following the peak of the X-ray emission, there is a rapid drop in luminosity exceeding 2 orders of magnitude. This X-ray dropoff is accompanied by X-ray spectral hardening, followed by a plateau phase of 740 days. During this phase, the spectral index decreases from $6.2 \pm 1.1$ to $2.3 \pm 0.4$, while the disk temperature remains constant. Additionally, we detect pronounced X-ray variability, with an average fractional rms amplitude of 47%, manifesting over timescales of a few dozen minutes. We propose that this phenomenon may be attributed to intervening clumpy outflows. The overall properties of AT 2019avd suggest that the accretion disk evolves from a super-Eddington to a sub-Eddington luminosity state, possibly associated with a compact jet. This evolution follows a pattern in the hardness–intensity diagram similar to that observed in stellar-mass BHs, supporting the mass invariance of accretion–ejection processes around BHs.

*Unified Astronomy Thesaurus concepts:* High energy astrophysics (739); Black holes (162); Accretion (14)

## 1. Introduction

Accretion processes have been studied in systems ranging from stellar-mass to supermassive black holes (SMBHs; masses $>10^5\,M_\odot$), spanning up to 8 orders of magnitude in mass (e.g., Rees 1984; Fender & Belloni 2004; Remillard & McClintock 2006; King & Pounds 2015; Gezari 2021). At the lower end of the mass range and at sub-Eddington accretion rates, we find BH X-ray binaries (BHXRBs). These systems are mostly transients that are only observable when they are in a short-lived outburst, typically lasting for a few months to a few years (e.g., White & Marshall 1984; Hjellming et al. 1999; Homan et al. 2003; Belloni et al. 2005). Two main spectral states have been defined based on the co-evolution of two X-ray spectral components: an accretion disk and a corona. In such systems, a hard state is defined when the nonthermal/Comptonization emission from a corona dominates the spectrum, while a soft state is defined when the thermal disk emission dominates the spectrum (see Remillard & McClintock 2006 for a review). Moreover, high variability represented by a fractional rms of ∼20%–40% has been commonly observed in X-rays in the hard state, while it decreases to $\lesssim$5% in the soft state (Gleissner et al. 2004; Muñoz-Darias et al. 2011). State transitions occur as the dominant component evolves from the Comptonization to the thermal component or vice versa.

As the mass accretion rate further increases, the system enters the so-called super-Eddington regime, in which intense radiation pressure is expected to drive powerful winds off the disk (e.g., Middleton et al. 2015b; Pinto et al. 2016), which has also been demonstrated by theoretical works (e.g., Shakura & Sunyaev 1973; Lipunova 1999) and numerical simulations (e.g., Narayan et al. 2017). Most ultraluminous X-ray sources (ULXs; Kaaret et al. 2017) are thought to be accreting in such a regime, making them ideal laboratories to study sustained super-Eddington accretion, given their close proximity ($\lesssim$ 17 Mpc). As opposed to BHXRBs, they are in general

persistent systems and show a variable-when-softer behavior (Middleton et al. 2011, 2015a; Sutton et al. 2013). Although the spectral states are defined differently from BHXRBs, state transitions have also been observed in such systems and have been associated with changes of the mass accretion rate and the opening angle of the supercritical funnel formed by the winds (Sutton et al. 2013; Middleton et al. 2015a; Gúrpide et al. 2021).

At the higher end of the mass range, SMBHs have been argued to be a scaled-up version of BHXRBs. However, the long evolutionary timescale (hundreds of thousands of years) of SMBHs hinders the making of direct observational comparisons. Nuclear transients such as tidal disruption events (TDEs), occurring in the vicinity of SMBHs, are key to solving this issue. The evolution of TDEs across the electromagnetic spectrum occurs on observable timescales, i.e., months to years, which makes them a perfect target for understanding the impact of BH mass on accretion processes in both the super- and sub-Eddington regimes.

Hills (1975) predicted that a TDE occurs when a star is disrupted by the gravitational tidal forces of an SMBH with a mass of $10^6$–$10^8\,M_\odot$. More than 20 yr later, such candidates were detected in X-rays with ROSAT by Komossa & Bade (1999). With the implementation of multiwavelength widefield surveys, the discovery pace of TDEs has accelerated dramatically (around 100 candidates as of now); of these, most are optically/UV selected, while ∼30% have shown X-ray emission and around a dozen have been detected in radio (see Alexander et al. 2020; van Velzen et al. 2020; Gezari 2021; Saxton et al. 2021 for reviews).

In the optical band, TDEs are characterized by their extreme variability on long-term (months-to-years) timescales, large peak luminosities (up to $10^{45}\,\mathrm{erg\,s^{-1}}$), and complex optical spectral features (e.g., transient H$\alpha$/He II/Bowen fluorescence emission lines; e.g., Gezari et al. 2012; Blagorodnova et al. 2018; van Velzen et al. 2021). TDEs are sometimes accompanied by ultrasoft X-ray emission. Unlike their smooth evolution in the optical, their behavior in X-rays is more complex and varies from system to system. The X-ray spectrum of TDEs can be described by either a blackbody component with $kT_{\rm bb} = 40$–$250\,\mathrm{eV}$ or a steep power-law component with $\Gamma > 4$ (e.g., Komossa & Bade 1999; Auchettl et al. 2017). There are a handful of systems that exhibit additional spectral features, such as ASASSN−14li (Miller et al. 2015; Kara et al. 2018), Swift J1644 + 57 (Kara et al. 2016), and AT2021ehb (Yao et al. 2022). In ASASSN−14li, highly ionized and blueshifted narrow absorption lines have been discovered in its high-resolution spectra (Miller et al. 2015). Kara et al. (2018) have also identified broad (∼30,000 km s$^{-1}$) features that were interpreted as an ultrafast outflow with a velocity of $0.2c$. In Swift J1644 + 57, Kara et al. (2016) observed a redshifted iron K$\alpha$ line in the 5.5–8 keV energy range, which was considered as evidence of disk reflection. In AT2018fyk, its spectrum shows both a soft excess and a hard tail in 0.3–10 keV; a state transition has also been observed, where the spectrum changes from disk-dominated to power-law-dominated when $L_{\rm bol} \sim 0.02\,L_{\rm Edd}$ (Wevers et al. 2021).

The flares of TDEs do not always decline smoothly, but are accompanied by relatively short-term X-ray variability (e.g., Saxton et al. 2012b; Pasham et al. 2023). Such variability has been observed on timescales of hundreds to thousands of seconds, e.g., millihertz quasiperiodic oscillations (QPOs; Reis et al. 2012; Pasham et al. 2019), submillihertz time lags (Kara et al. 2016; Jin et al. 2021), dips with peculiar patterns in the lightcurve (Saxton et al. 2012b), and variability associated with a softer-when-dimmer behavior (Lin et al. 2015). Interestingly, Pasham et al. (2019) discovered a stable 131 s QPO in ASASSN–14li, whose frequency is comparable to the millihertz QPOs observed in BHXRBs (e.g., Altamirano & Strohmayer 2012) and ULXs (e.g., Strohmayer & Mushotzky 2003; Mucciarelli et al. 2006), but in softer X-rays (0.3–1 keV). This discovery disfavors the correlation between the QPO and hard X-rays, and the QPO mass scaling.

A peculiar nuclear transient AT 2019avd, located at $z = 0.028$, has been detected from radio to soft X-rays. This transient was first discovered in the optical by the Zwicky Transient Facility (ZTF; Bellm et al. 2019), and the overall outburst has shown two continuous flaring episodes with different profiles, spanning over 2 yr. The X-ray flare was first detected by Spectrum-Roentgen-Gamma/eROSITA during the second episode and had been continuously monitored by Swift and NICER. It is unclear when the X-ray activity was triggered, but several works have suggested that it was later than the optical (Malyali et al. 2021; Chen et al. 2022; Wang et al. 2023). The ultrasoft X-ray spectrum and optical spectral lines of AT 2019avd are consistent with a TDE, but the two consecutive optical flares are atypical of TDEs. In addition, Wang et al. (2023) report the radio detection of this transient with the Very Large Array and Very Long Baseline Array (VLBA), suggesting the possible ejection of a compact radio outflow (jet or wind) when the sources moved to a low-luminosity state.

The multiwavelength study of AT 2019avd has been reported in Wang et al. (2023). In this work, we focus on exploring in depth its X-ray temporal and spectral properties, with proprietary NICER and Chandra observations, and archival data from Swift, which were performed ∼459 days after the ZTF detection. The paper is structured as follows: in Section 2, we describe our observations and data reduction; in Sections 3 and 4, we present and discuss, respectively, the overall evolution of the X-ray properties; and in Section 5, we conclude and highlight the main results of our work.

## 2. Observations and Data Reduction

In this paper, uncertainties and upper/lower limits are quoted at the $1\sigma$ and $3\sigma$ confidence levels, respectively. We adopt a redshift of 0.028, based on the report from the Transient Name Server,[17] a luminosity distance of $D = 130$ Mpc from Wang et al. (2023), and a BH mass $M_{\rm BH}$ of $10^{6.3}\,M_\odot$ from Malyali et al. (2021). We also adopt the Galactic absorption of $2.4 \times 10^{20}\,\mathrm{cm^{-2}}$ from the HI4PI survey (HI4PI Collaboration et al. 2016) as the lower limit of the column density of AT 2019avd.

### 2.1. X-Ray Telescope/Swift

Swift has performed 51 observations on this source from 2020 May 13 to 2022 May 26. We used the 45 X-ray Telescope (XRT) observations, in photon counting mode, with a total exposure time of 56.4 ks.

[17] https://www.wis-tns.org/object/2019avd

The XRT data were reduced with the tasks XRTPIPELINE and XSELECT. The source and background events were extracted using a circular region of 40″ and an annular ring with inner and outer radii of 60″ and 110″, respectively, both centered at the position of the source. The Ancillary Response Files (ARFs) were created with the task XRTMKARF and the Response Matrix File (RMF) used was swxpc0to12s6_20130101v014.rmf, taken from the Calibration Database (CALDB).[18] Due to the small numbers of counts, the XRT spectra were grouped to have a minimum of 3 counts[19] per bin using the FTOOL GRPPHA. Consequently, W-stats was used for the spectral fitting. Since the source is background-dominated above 2 keV, we only fitted the XRT spectra in 0.3–2 keV, which can be described well with an absorbed blackbody component until the late time (MJD 59483) of the flare. Additionally, we calculate the hardness ratio of the count rates in 0.8–2.0 keV over that in 0.3–0.8 keV.

### 2.2. Low Energy Transmission Gratings/Chandra

AT 2019avd was observed twice with Chandra Low Energy Transmission Gratings (LETGs) on 2021 June 8 and 9 (ObsIDs 25056 and 25060; PI: Pasham), with a total exposure time of 50 ks. The data were reduced using CIAO[20] version 4.13 and CALDB version 4.9.5. We first reprocessed the data with the script CHANDRA_REPRO to generate new level 2 event files. We then ran the tool TGDETECT to determine the source position in the Chandra image. However, we detected no source with significance $>2\sigma$, which suggests that the source is too faint for a further spectral analysis. Alternatively, we ran SRCFLUX to estimate the source flux centered on the source location, by assuming an absorbed `powerlaw`[21] spectrum with $\Gamma = 2$ in the 0.7–10 keV band. The value of $\Gamma$ is inferred from the latest NICER spectrum. We obtained a luminosity of $(5.7\text{–}8.0) \times 10^{41}$ erg s$^{-1}$ at the time of the Chandra observations.

### 2.3. X-Ray Timing Instrument/NICER

NICER performed high-cadence monitoring observations of AT 2019avd with the X-ray Timing Instrument (XTI) from 2020 September 19 until 2021 June 16, split across 207 observations, with a cumulative exposure time of approximately 408.5 ks. We reprocessed the data using the NICERDAS version of 2020 April 23 and CALDB version xti20200722. In addition to the standard data reduction steps of filtering, calibrating, and merging the NICER events, we excluded some XTI detectors on an observation basis when the count rates deviated $>3\sigma$ from the mean or were switched off during the observations. Additionally, Focal Plane Modules 14 and 34 are always excluded, since they often exhibited episodes of increased detector noise. We applied the tool NIBACKGEN3C50 (Remillard et al. 2022) with level 3 filtering criteria, i.e., $hbgcut = 0.05$ and $s0cut = 2$, to extract and estimate the NICER spectra and background. The RMFs and ARFs tailored for the selected detectors were applied in the spectral analysis. Finally, all the spectra were grouped with FTGROUPPHA, using the optimal binning scheme (Kaastra & Bleeker 2016). We also excluded some NICER observations when (i) the exposure time was shorter than 100 s; (ii) the background and/or the contamination (see the next paragraph) were higher than the source flux above 1.7 keV; and (iii) the observations were performed after MJD 59360 (these observations are mostly contaminated by Sun glare). In the end, we obtained 153 NICER observations for further analysis. Similar to the XRT spectra, there is no significant emission above 2 keV, so we only fit the NICER spectra in the 0.3–2 keV band. We also calculated the hardness ratio with the NICER data using the same energy bands applied to the XRT data.

Additionally, there is another persistent X-ray source, IC 505, at a distance of about 3.′7 from AT 2019avd in the large field of view (FOV) of XRT. We compare the position of this contaminating source with NICER's FOV with a radius of 3.′1 (Wolff et al. 2021; Pasham et al. 2022) and find that this source is located on the edge of NICER's FOV. As observed by both XMM-Newton/EPIC-pn in 2015 and Swift/XRT in 2019–2022, IC 505 appears to be stable over time (see Figure A1), with a `powerlaw` spectrum plus an emission line around 1 keV, whose flux is $\sim 0.3 \times 10^{-12}$ erg cm$^{-2}$ s$^{-1}$ in 0.3–2 keV. Based on this flux level, we determined that part of the emission in the NICER observations of AT 2019avd is contaminated by IC 505. However, owing to the stability of the flux of IC 505, we were able to subtract its contribution from the NICER data of AT 2019avd (the method is described in detail in Appendix A).

## 3. Results

### 3.1. Flare Evolution

We show the long-term X-ray lightcurve of AT 2019avd in Figure 1(a). The NICER, Swift, and Chandra data are labeled as black dots and light blue and red stars, respectively. The first detection of the NICER campaign, MJD 59110, which refers to the peak of the flare in X-rays, is defined as Day 0. In Figure 1(b), the black dots and the light blue stars denote the hardness ratio derived from the NICER and Swift observations, respectively.

To better describe and locate the evolution of the flare in different periods, we divided the entire lightcurve into six phases, which are marked with Arabic numerals from 0 to 5 and are separated with vertical dashed lines in Figure 1. Phases 0 and 5 correspond to the periods prior to and after the flare, respectively, without NICER observations, while phases 1 to 4 correspond to Days 0–100, 101–172, 173–225, and 226–249, respectively. The evolution of the flare can be described as follows.

In phase 0, the luminosity first increased by more than an order of magnitude and peaked around Day 0. In phase 1, the luminosity decreased by nearly a factor of 5, while the hardness ratio remained constant. During phase 2, the luminosity reached another peak and the hardness ratio gradually increased. In phase 3, the luminosity decreased rapidly by an order of magnitude and the hardness ratio increased. Later, in phase 4, the source continuously dimmed, while the hardness ratio increased. Right after phase 4, AT 2019avd went into Sun glare afterward for NICER. Follow-up XRT and LETG observations between Days 258 and 267, 9 days after phase 4, show a further decrease in the source flux. After the seasonal gap (between Days 266 and 373) in phase 5, the X-ray

[18] https://heasarc.gsfc.nasa.gov/docs/heasarc/caldb/swift

[19] https://giacomov.github.io/Bias-in-profile-poisson-likelihood

[20] https://cxc.cfa.harvard.edu/ciao

[21] As reported by Wang et al. (2023) and our analysis of the Swift and NICER data, the spectrum hardened as the luminosity decreased. We hence assumed a power-law spectrum to estimate the current flux.

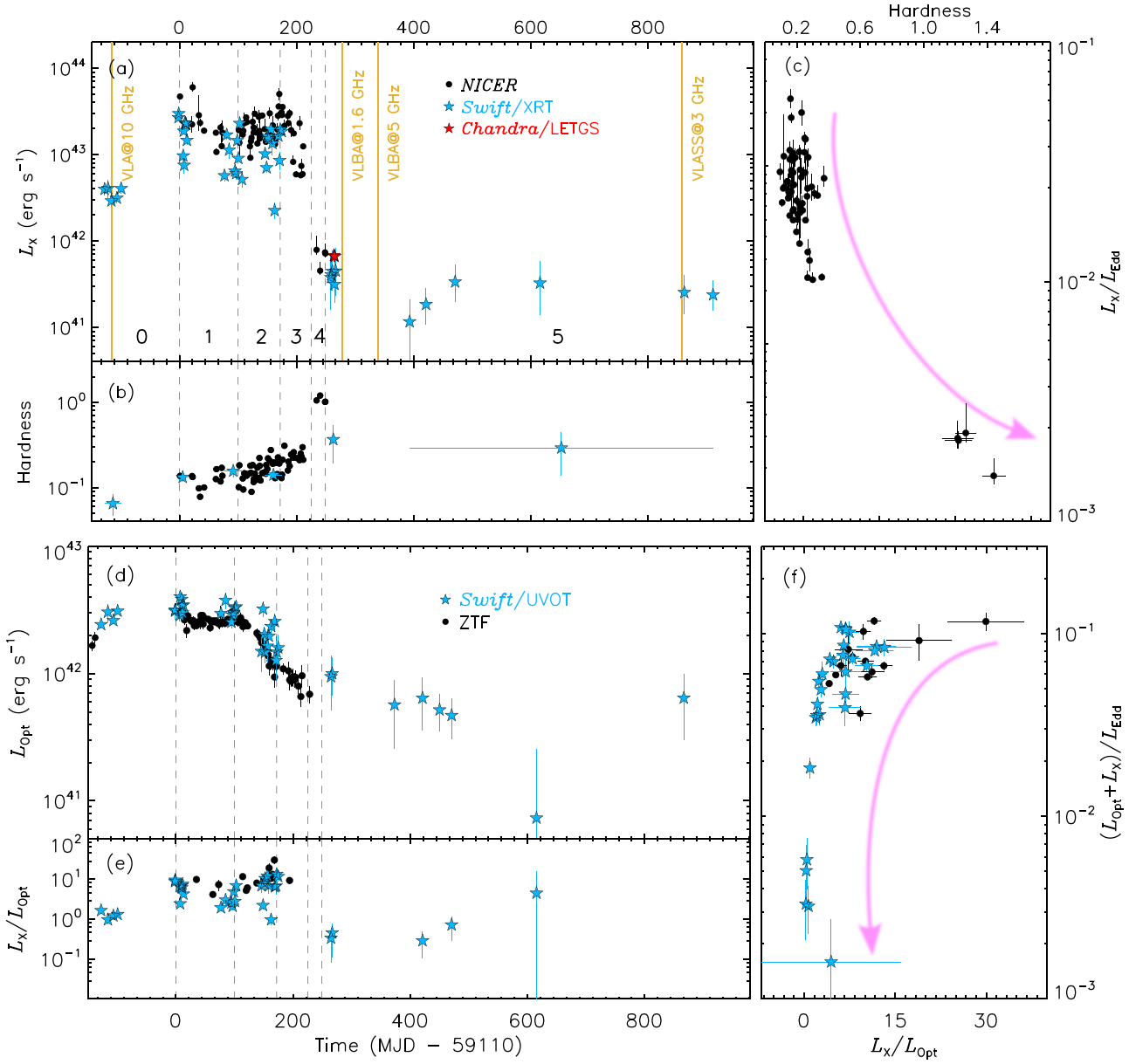


**Figure 1.** (a) Unabsorbed X-ray luminosity in the 0.3–2 keV band. The black dots, light blue stars, and red stars represent the NICER, XRT/Swift, and LETG/Chandra data, respectively. The yellow vertical lines indicate where there are radio detections (taken from Wang et al. 2023, except the last VLASS detection). The vertical dashed lines divide the flare into six phases, each identified by a number. (b) The evolution of the hardness ratio of the 0.8–2.0 keV count rate with respect to the 0.3–0.8 keV count rate (background excluded). To increase the signal-to-noise ratio of the XRT hardness ratio, we combine the data into six groups. (c) HID using NICER data. (d) Optical and UV lightcurves. The black dots and blue stars show the optical data in the $g$ band of ZTF and the UV data in the UVW1 band of UVOT/Swift, respectively. The optical and UV data are taken from Wang et al. (2023), both of which are host-contribution-subtracted and Galactic-extinction-corrected. (e) The X-ray-to-optical/UV ratio. The dots and stars represent the ratios of NICER to the ZTF $g$ band and of XRT/Swift to the UVW1 band of UVOT. (f) The X-ray-to-optical/UV ratio vs. the bolometric luminosity. The light blue arrows denote the upper limits of the detection at a $3\sigma$ confidence level. The magenta arrows indicate the temporal evolution of the ratios.

luminosity remained the same as in phase 4 and lasted for over ∼700 days, the flux being more than 2 orders of magnitude lower than the peak of the flare in phase 1.

Compared to NICER, XRT has a relatively smaller effect area; also, the XRT observations were either of relatively short exposure time or were performed when the source was relatively faint ($L_X < 10^{43}$ erg s$^{-1}$). To increase the signal-to-noise ratio of the hardness ratio, we divided the whole XRT data set into six groups, based on the observation time, and combined the data from each group to calculate the hardness ratio. We added the XRT hardness as the light blue stars to Figure 1(b), in which the error bars along the $x$-axis indicate the duration of each group. The XRT hardness shows a comparable evolution to the NICER hardness and further increases after the NICER campaign (we only compare the hardness ratios derived from the same instrument).

The NICER hardness–intensity diagram (HID) is shown in Figure 1(c): the hardness ratio remained nearly constant as the luminosity decreased in phases 1–3, then increased as the luminosity further decreased in phase 4. We convert the luminosity to units of Eddington luminosity ($L_{Edd}$), which peaks around 0.24 $L_{Edd}$.

Figure 1(d) shows the optical and UV photometries derived from the $g$ band of ZTF and the UVW1 band of Swift with

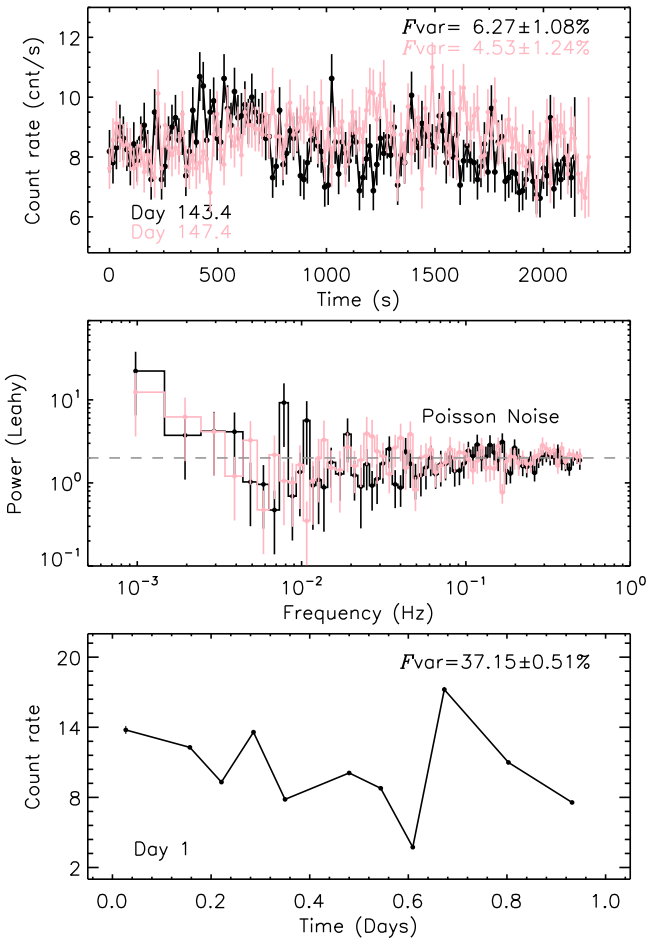


**Figure 2.** Top: examples of lightcurves in bins of 16 s. Middle: the corresponding periodogram of the above lightcurves. The dashed line shows a Poisson noise level of 2. Bottom: an example of a lightcurve in bins of GTI.

symbols of dots and stars. These data are taken from Wang et al. (2023) and have been corrected for the Galactic extinction and contribution from the host galaxy. Figure 1(e) shows the X-ray-to-optical/UV luminosity ratio: the dots represent the ratios of luminosity inferred from NICER and ZTF, and the stars represent the ratios of luminosity inferred from XRT and UVOT. The trends of the two curves are consistent when the observations are quasi-simultaneous. Figure 1(f) shows the X-ray-to-optical ratio as a function of the bolometric luminosity, which is taken as the sum of the optical/UV and X-ray luminosities. Similar to the trend of the HID curve shown in Figure 1(c), the X-ray-to-optical ratio decreases as the bolometric luminosity decreases.

### 3.2. X-Ray Timing Properties

As shown in Figure 1(a), the X-ray emission is highly variable. To quantify the variability, we first generated power spectral densities (PSDs) with Leahy normalization (Leahy et al. 1983). Since the durations of the NICER Good Time Intervals (GTIs) range between 18 and 2146 s, the frequency of the periodogram can only be traced down to ∼0.5 mHz. We show two examples of the lightcurves with longest duration and the corresponding periodogram with a frequency range of 1–500 mHz in Figure 2. There is no periodic signal present in either periodogram, but the power of the periodogram tends to increase toward lower frequencies. As a comparison, we show an example of a lightcurve spanning roughly one day in the bottom panel of Figure 2, in which the flux variation is much larger. These suggest that the variability of AT 2019avd dominates over longer timescales.

To further explore the short-term variability over a longer duration, we generated the background-subtracted lightcurve in bins of GTI and then computed the excess fractional rms variability amplitude, $F_{\rm var}$, between the GTIs of each observation (see Appendix B for more details on the calculation). To reduce the bias of the length of the individual observations, we chose only observations lasting longer than 10 ks with more than four GTIs. Equation (B2) shows that the $F_{\rm var}$ of each individual observation can only be computed if the variance is larger than the measured errors. Thus, we ignored the data that do not fulfill this criterion. The absolute rms amplitude, $\sigma_{\rm XS}$, was computed as $F_{\rm var}$ multiplied by the mean count rate of an observation.

As illustrated in Figure 2, the variability on a timescale of minutes is significantly higher than that on a timescale of seconds, e.g., $F_{\rm var}$ increases by a factor of 6–8. We further plot $\sigma_{\rm XS}$ and $F_{\rm var}$ as a function of the count rate in Figure 3. $F_{\rm var}$ is quite high and scattered, ranging between 12.6% and 105.1%, with an average of 47% (42% in phases 1–3 and 65% in phase 4). $\sigma_{\rm XS}$ is strongly correlated to the count rate, while the correlation between $F_{\rm var}$ and count rates shows an opposite trend, $F_{\rm var}$ decreasing with increasing flux. We fitted a power law and a linear model to each curve of NICER shown in Figure 3 and found that the dots in phase 4 deviate from the linear fits of both curves.

To test the validity of the high $F_{\rm var}$, we applied the same method to the XRT data. Given that most of the XRT observations consist only of one GTI, we computed the $F_{\rm var}$ of the XRT data within a GTI (in bins of 128 s). Due to the low statistics, we were only able to measure the $F_{\rm var}$ of 16 GTIs in phases 1–3. We added the results as light blue diamonds, together with measurements of the average (marked with magenta stars in Figure 3). Although with considerable uncertainties, the $F_{\rm var}$ values derived from the XRT data are consistent with the NICER data. Even though the $F_{\rm var}$ values from the NICER data could be overestimated/underestimated, as the GTIs are not evenly sampled, the comparable values of $F_{\rm var}$ provided by XRT support the high variability detected by NICER.

To show the relation between $F_{\rm var}$ and the spectral state, we plot $F_{\rm var}^2$ against the spectral hardness in the middle panel of Figure 3, in which $F_{\rm var}^2$ increases with the hardness. The overall curve can be described by a broken power law with two regions, and the inflection point corresponds to where the state transition occurs. More specifically, the left side (hardness $< 0.4$) of the curve is relatively soft and occupied by the data in phases 1–3, with an increase in variability with increasing hardness, while the right side (hardness $> 0.4$) is hard and occupied by the data in phase 4, with a further increase in variability as the spectrum hardens.

To further explore the energy dependence of the variability, we computed $F_{\rm var}$ spectra and illustrate them in the right panel of Figure 3. In phases 1–3, $F_{\rm var}$ increases with energy until 1 keV and then show some wiggles at higher energies, indicating that the rms spectrum consists of two components. Conversely, the values of $F_{\rm var}$ in phase 4 are higher than at the other phases, showing invariant evolution at energies below 1 keV and diminishing at higher energies.

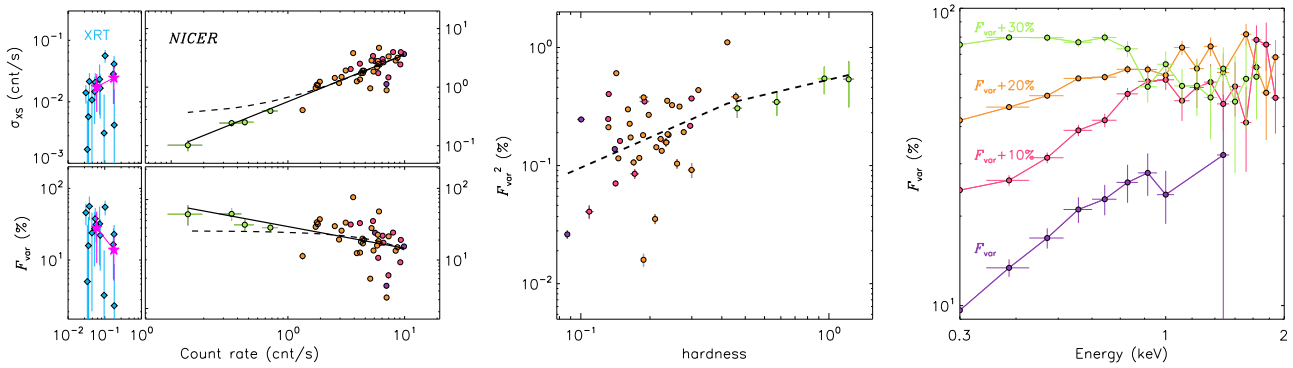


**Figure 3.** Left: absolute and fractional rms amplitude vs. count rate. The magenta stars represent the rebinning of the XRT data. The solid and dashed lines indicate the power-law and linear fits, respectively, to the data of NICER. The purple, magenta, yellow, and green dots correspond to phases 1–4, respectively. Middle: fractional rms amplitude vs. hardness. Right: fractional rms amplitude vs. energy. The offsets of $F_{\rm var}$ are labeled.

### 3.3. X-Ray Spectral Properties

We study the flux-averaged X-ray spectrum in units of observation in this section. The spectrum is ultrasoft, being background-dominated above 2 keV during the flaring episode. The XRT spectrum can be reasonably described by an absorbed `bbody` until phase 5, when an absorbed `powerlaw` is required instead. Compared to XRT, the NICER spectra show more complex features, requiring two components in most cases. As the best-fitting parameters of the XRT spectrum have already been shown in Wang et al. (2023), we focus on the NICER spectra in this work.

To describe the NICER spectra, we employed a phenomenological model including one absorbed `bbody` component plus a `powerlaw` component. The redshift of the galaxy was taken into account by an additional `zashift` component that was fixed at 0.028. In addition to the two continuum components, there is an emission-line feature below 1 keV or an absorption-line feature above 1 keV in the individual observations. Unfortunately, the emission line is also present in the spectrum of IC 505, making it difficult to associate it with AT 2019avd and hence we do not investigate it further. As for the absorption line, we show an example of the unfolded spectrum in Figure C1 without and with the contamination from IC 505. An absorption line with a centroid energy of $1.03 \pm 0.01$ keV is clearly present in the spectrum, which may indicate the presence of disk winds.

Figure C1 also shows the continuum components. The soft excess, modeled with `bbody`, is significantly required in phases 1–3. In phase 4, only one component is required. Either a `powerlaw` or a `bbody` can describe the data, but the former always provides a statistically better fit than the latter, i.e., obtaining a smaller $\chi^2$. This has also been mentioned in Wang et al. (2023), i.e., they were unable to statistically distinguish whether the spectrum was thermal or nonthermal at the beginning of phase 5; however, the spectrum clearly flattened later (i.e., Days 373–615; see Figure 4 of Wang et al. 2023). This evidence suggests that the source evolved from a `bbody`-dominated/soft state (phases 1–3) to a `powerlaw`-dominated/hard state (phases 4–5). The state transition occurred around $L_X \sim 0.01\, L_{\rm Edd}$.

We plot the evolution of the best-fitting parameters and the individual flux of the continuum components in Figure C2. The full description of the spectral evolution is presented in Appendix C. We further plot the blackbody temperature and the photon index in phases 1–3 as a function of the luminosity in Figure 4. As the luminosity decreases by over 1 order of magnitude, the blackbody temperature remains constant and the photon index decreases with the luminosity.

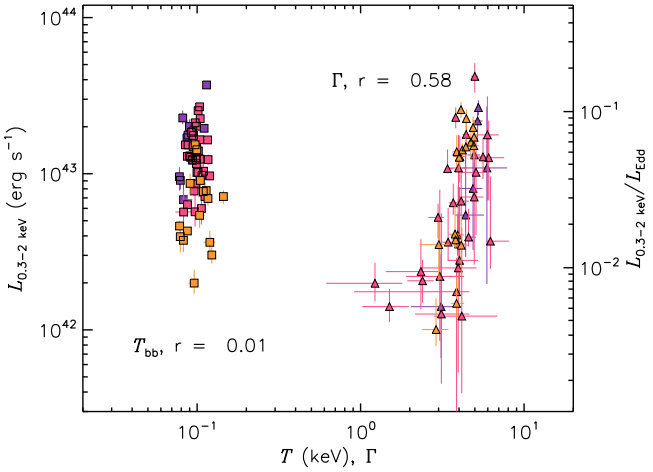


**Figure 4.** Blackbody temperature/photon index vs. the `bbody` and the `powerlaw` luminosity, respectively. $r$ represents the linear Pearson correlation coefficient. The colors are defined in the same way as in Figure 3.

Additionally, to explore the properties of any outflowing materials via the absorption feature, we generated a grid of photoionization models with varying column density ($N_{\rm gas}$) and ionization parameter ($\log \xi_{\rm gas}$) with XSTAR (Kallman & Bautista 2001). We assumed a `bbody` spectrum with a temperature of 0.1 keV and a luminosity of $2.0 \times 10^{43}$ erg s$^{-1}$ (integrated from 0.0136 to 13.6 keV), irradiating some materials with a fixed gas density of $10^{10}$ cm$^{-3}$, a turbulent velocity of $10^5$ km s$^{-1}$ (based on the width of the line), and solar abundances. We replaced `gaussian` with `xstar` and obtained a fit with $\chi^2/\nu = 20.25/19$. The latter reveals $N_{\rm gas} = 2.5 \pm 0.2 \times 10^{23}$ cm$^{-2}$, $\log\ \xi_{\rm gas} = 3.44^{+0.28}_{-0.12}$ erg cm s$^{-1}$, and a blueshifted velocity of $0.08 \pm 0.02c$. Hence, the absorption feature could be due to Ne IX, Fe XIX, Fe XX, or a mixture of several of them. Further discrimination cannot be achieved with the spectral resolution of the data.

## 4. Discussion

We have used the NICER, Swift, and Chandra observations to study the accretion and ejection properties of the highly variable nuclear transient AT 2019avd. The X-ray flaring episode lasted for over 1000 days, spanning over 2 orders of magnitude in luminosity. A rapid decrease in the luminosity

was observed at ∼225 days after the peak of the X-ray flare, followed by a state transition occurring at $0.01\,L_{\rm Edd}$. In the following, we discuss the X-ray variability, the possible physical origins of the soft excess with a constant temperature, the potential triggers for the state transition, and eventually compare our target with other accreting BHs.

### 4.1. Evolution of the X-Ray Variability

The linear absolute rms–flux relation has been observed in all types of accreting systems (e.g., Uttley & McHardy 2001; Vaughan et al. 2003; Heil & Vaughan 2010; Scaringi et al. 2012) and has been interpreted as a result of inwardly propagating variations via accretion flows (Lyubarskii 1997). In the case of AT 2019avd, although with some scatters, the absolute rms–flux relation shows deviations from linearity in phase 4 (see Figure 3). Together with the fractional rms–flux relation, this suggests that either the intrinsic variations of the emission in phases 1–3 and 4 are different and/or the geometry of the accretion flow has changed, e.g., from a slim to a thick disk. We discuss these possibilities below.

As shown in Figure 3, the fractional rms amplitude $F_{\rm var}$ of AT 2019avd is very high, with an average of 43%, and its evolution is related to the spectral state. Such a high variability has only been observed in limited accreting systems, for instance the BHXRB GRS 1915 + 105 (Fender & Belloni 2004) and ULXs NGC 5408 X–1 and NGC 6946 X–1 (Middleton et al. 2015a; Atapin et al. 2019). The common properties of these targets are super-Eddington accreting rates with strong outflows. Although the X-ray luminosity of AT 2019avd is below the Eddington luminosity, based on the fit to the broadband spectral energy distribution (SED) from optical to X-rays, Wang et al. (2023) found the bolometric luminosity to be $6.7\,L_{\rm Edd}$,[22] suggesting that AT 2019avd is in the super-Eddington regime in phases 1–3.

Middleton et al. (2015a) have proposed a spectral timing model, taking into account both the intrinsic variability via propagated fluctuations and the extrinsic variability via obscuration and scattering by winds to explain supercritically accreting ULXs. In this scenario, the evolution of the overall variability and the spectral hardness is suggested to be determined by the changes in two parameters: the mass accretion rate and inclination angle. The latter may vary due to precession of the accretion disk. Under this framework, the evolution of $F_{\rm var}$ against the hardness of AT 2019avd is consistent with the mass accretion rate decreasing while the inclination angle either decreases or remains constant. More explicitly, when the disk inclination angle is moderate[23] and the mass accretion rate is high, disk winds would have a small opening angle toward the observer and thus have a higher probability of intercepting the high-energy emission from the hot inner disk. This would result in a softer spectrum and highly variable hard X-rays via obscuration and scattering. While either the mass accretion rate and/or the inclination angle decrease, the opening angle of the disk winds toward the observer increases and more of the hot inner disk would be exposed directly to the observer. Subsequently, the dominant emission will harden and exhibit reduced variability, due to the decrease in obscuration and scattering, at odds with the further increase of the variability and the dimming of the target in phase 4. Even in phase 5, AT 2019avd remains highly variable (see the green dots in the rightmost panel of Figure A1). In fact, ULXs are persistent sources, such that we should not expect transients like AT 2019avd to share all the properties of ULXs, especially after the abrupt decrease in the mass accretion rate in phase 4.

To examine whether the variability can be attributed to the existence of a local absorber, potentially leading to increased absorption or obscuration, we divided the XRT data in phases 1–3 into two segments, based on the luminosities exceeding and falling below $10^{43}\,{\rm erg\,s^{-1}}$. Then we jointly fitted the spectra from the two segments with an absorbed `bbody` component plus a `powerlaw` component. To improve the constraint on $N_{\rm H}$, both $kT_{\rm in}$ and the `powerlaw` component are linked to vary across observations. We verified the necessity of the power-law component for both segments using the FTEST command. The null probability for the high-flux segment is $9.4\times10^{-9}$ and for the low-flux segment it is $7.7\times10^{-5}$. Next, we compared the values of $N_{\rm H}$ obtained from the fits with and without the `powerlaw` component. Interestingly, we found that for the low-flux segment, $N_{\rm H}$ tends to be slightly higher, while the power-law flux is lower. However, the disparity in $N_{\rm H}$ values between the two segments remains consistent within uncertainties, specifically $1.03\pm0.52\times10^{21}\,{\rm cm^{-2}}$ and $0.63\pm0.28\times10^{21}\,{\rm cm^{-2}}$. In summary, these results may suggest the presence of a local absorber, but a more definitive conclusion is hampered by the data quality.

Alternatively, the evolution of $F_{\rm var}$ against the hardness/count rate is consistent with the one seen in BHXRBs when a source evolves from a relatively soft to a hard state during the decaying phase of an outburst (e.g., Stiele & Kong 2017; Wang et al. 2020; Alabarta et al. 2022). The temporal evolution of the hardness and the flux of AT 2019avd, as well as the HID curve and the radio emission detected in phase 5, are also in good agreement with the decaying phase of an outburst and the launch of a jet of BHXRBs. Considering the data used for the computation of $F_{\rm var}$, the corresponding frequency range would be roughly 10–100 $\mu$Hz, which could be converted to $1-10$ Hz for a stellar-mass BH of $10\,M_{\odot}$. However, the fractional rms in such a frequency range of BHXRBs is normally 15%–30% (e.g., Heil et al. 2012; Wang et al. 2020). This unusually high rms makes AT 2019avd different from typical sub-Eddington accreting BHs.

Short-term variability on timescales of hundreds to thousands of seconds has been explored in several TDEs, such as Swift J1644 + 57 (Reis et al. 2012; Saxton et al. 2012a), ASASSN–14li (Pasham et al. 2019), etc. Such short timescales indicate that the X-ray-emitting region of TDEs is compact, e.g., $3\times10^{12-13}$ cm. AT 2019avd tends to show both small variations on timescales of hundreds of seconds (see Figure 2) and large variations on timescales of thousands of seconds (see Figure 3). The latter is revealed by the presence of dips. Saxton et al. (2012a) observed a dipping behavior with peculiar patterns in the brightest relativistic TDE Swift J1644 + 57. The spectrum softened during the dips without requiring changes in column density. This evidence supports their idea that the dips were driven by the precession and nutation of jets.

[22] It is worth noting that the absence of extreme UV emission results in a consistent underestimation of the observed luminosity in both the optical/UV and X-ray spectra. However, it is crucial to note that the SED modeling discussed in Wang et al. (2023) incorporates significant absorption at the AT 2019avd location, a factor that is not considered in the current study. Therefore, caution is advised when interpreting the absolute value of the bolometric luminosity in this context.

[23] If the scale height of the disk is large, a small inclination angle may also work.

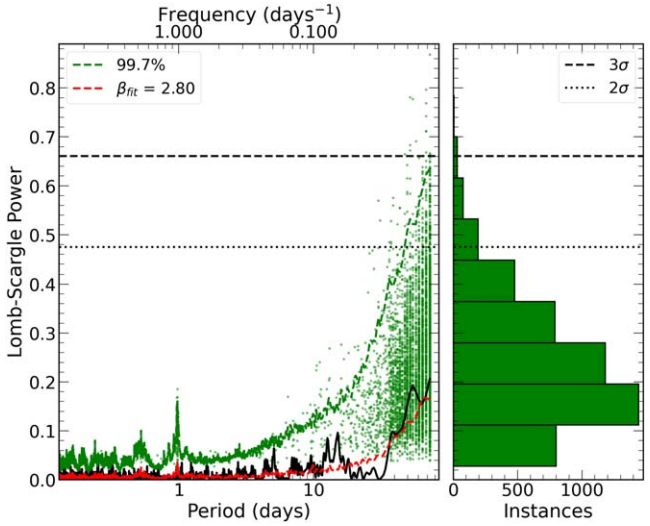


**Figure 5.** Lomb–Scargle periodogram of the NICER data (solid black line), with the green dashed line showing the one-trial $3\sigma$ false-alarm probability, while the multiple-trial $2\sigma$ and $3\sigma$ false-alarm probabilities are shown by the black dotted and dashed lines, respectively. The red line represents the average of the simulated periodograms. The scattered green dots and the right panel show the position (in frequency) and distribution of the maximum peaks in the simulated lightcurves.

Recently, Chen et al. (2022) proposed that the X-ray variability of AT 2019avd could be due to Lense–Thirring precession of the accretion disk and predicted a precession period of 10–25 days. In order to test whether the variability is associated with precession, we conducted lightcurve simulations to infer the PSDs of the source (taking into account gaps, aliasing, and red-noise leakage effects) and used such an estimate (and its uncertainties) as the null hypothesis to test for the presence of any significant peak in the (Lomb–Scargle) periodogram. We refer the reader to Appendix D for the details. The results are shown in Figure 5, which displays the $3\sigma$ one-trial (blue dotted line) and multiple-trial (green dashed line) false-alarm probabilities based on the inferred null hypothesis (red line). Overall, we find no obvious peak above the false-alarm probability levels. This is supported by the good agreement between the best-fit periodogram (red line) and the data (with a rejection probability of 50%; see Appendix D). We thus conclude that the variability of AT 2019avd is fully consistent with the typical aperiodic variability commonly observed in accreting systems.

Overall, we conclude that the high variability of the X-rays of AT 2019avd is very likely due to the presence of clumpy winds, and the state-/luminosity-dependent evolution of the variability in phases 1–3 could be interpreted by the decrease in the mass accretion rate and subsequent opening angle of the funnel of the supercritical disk. It remains unclear why AT 2019avd remains so variable even after the luminosity drops below 1% $L_{\rm Edd}$. It however should be noted that whether supercritical accretion can initiate clumpy winds is a topic of ongoing debate. Some 2D numerical simulations (e.g., Takeuchi et al. 2013, 2014) propose that super-Eddington clumpy winds might be induced by the Rayleigh–Taylor instability. On the other hand, some 3D simulations employing radiation magnetohydrodynamics or relativistic radiation magnetohydrodynamics (e.g., Jiang et al. 2014; Sadowski & Narayan 2016) suggest the opposite. The disk precession scenario cannot be completely ruled out, but its contribution to the observed variability should be limited.

### 4.2. Constant Blackbody Temperature

The evolution of thermal blackbody temperatures in TDEs has been extensively studied in the optical–UV bands, and they have shown different trends along with the flare (e.g., Hinkle et al. 2020; van Velzen et al. 2021; Hammerstein et al. 2023). Some of the temperatures are observed to remain roughly constant with small-scale variations, e.g., ASASSN–14li (Holoien et al. 2016) and ASASSN–18pg (Holoien et al. 2020), and some show either a decreasing or increasing trend (van Velzen et al. 2021). In one of the best-observed TDEs, ASASSN–14li, while the luminosity dropped nearly 2 orders of magnitude over 600 days, the blackbody temperature remained relatively constant in the optical/UV (Holoien et al. 2016) and decreased at most by a factor of 2 in the X-rays (Brown et al. 2017). Due to the scarce data sample of TDEs with X-ray emission, the evolution of the characteristic temperature in X-rays has not been statistically studied as much as in the optical–UV bands.

A soft excess has been detected at least in phases 1–3 of the X-ray flare of AT 2019avd. Irrespective of its physical origin, the soft excess can be well described by a `bbody` component. The obtained $T_{\rm bb}$ is rather stable during phases 1–3, while the luminosity decreases by over 1 order of magnitude. Figure 4 shows that the $T_{\rm bb}$–$L_{\rm bb}$ relation does not follow the $L \propto T_{\rm bb}^4$ scaling for an optically thick, geometrically thin accretion disk (Shakura & Sunyaev 1973). This means that the accretion disk of AT 2019avd is very unlikely to be thin.

A similar soft excess below 2 keV has been ubiquitously observed in active galactic nuclei (AGN) with low column densities (e.g., Singh et al. 1985), although the origin of this excess remains debated. We compare our result with the two most popular models for the soft excess in AGN: warm, optically thick Comptonization (e.g., Gierliński & Done 2004; Petrucci et al. 2018) and blurred ionized reflection (e.g., Ross & Fabian 1993; Ballantyne et al. 2001; Kara et al. 2016). To test the Comptonization scenario, we replaced the `bbody` component with a Comptonization component, `comptt`, and obtained a comparable fit. However, even for the spectra observed around the peak of the flare and with a long exposure time, the parameters of `comptt` cannot be constrained well. We then fixed $\Gamma$ of the `powerlaw` to the value derived from the original model to avoid model degeneracy, e.g., in the fit to the spectrum of ObsID. 3201770101 (the first observation of the NICER campaign, with an exposure time of 7.1 ks), the best-fitting value of $\tau$ is up to 0.3 at the $1\sigma$ confidence level, with the temperatures of the seed photon and the hot plasma being 100–102 eV and 7.1–10.8 keV, respectively. This value is much lower than the typical optical depth in AGN where $\tau = 10$–$20$, indicating that the required Comptonization region is optically thin instead of thick and hence inconsistent with this scenario. In the blurred ionized reflection scenario, if the soft excess is produced by the disk reflection from hard X-rays, i.e., the `powerlaw` component in our case, the `powerlaw` and `bbody` fluxes should be correlated. Even though they appear to be correlated in phase 3, they seem to be marginally anticorrelated in phase 2 (see Figure C2), at odds with this scenario. Overall, the soft excess observed in AT 2019avd cannot be solely interpreted by either of these two scenarios.

In fact, since the inner hot X-rays could have been obscured and scattered into softer X-rays or even UV emission, the observed soft excess would actually greatly deviate from physical reality. Recently, Mummery (2021) has described the impact of the use of a single-temperature blackbody, including the disk inclination angle and the local absorber, such as stellar debris and outflows, on the determination of the disk radius and temperature in the context of TDEs. They suggest that the disk temperature would have been overestimated/underestimated if neglecting the effect of the hardening factors/the local absorber. Due to the limited bandpass and the complexity of the spectrum of AT 2019avd, we do not explore more sophisticated models here, and the present disk temperature should be taken with caution. More data and theoretical work are needed to understand whether such a constant temperature in X-rays is due to observational/model effects and/or is driven by some physical mechanism, which are beyond the scope of this work.

### 4.3. Rapid Dimming in Luminosity

A fraction of TDEs experience abrupt dimming in X-rays, e.g., partial TDEs (Wevers et al. 2021, 2023; Liu et al. 2023) and jetted TDEs (Zauderer et al. 2013). Both of them present a similar rapid drop in X-ray luminosities as in AT 2019avd, along with a state transition.

Regarding partial TDEs, if one considers $\Gamma$ obtained from the `powerlaw` model, both the evolution and values for AT 2019avd are comparable to those observed for the partial TDE eRASSt J045650.3–203750 (Liu et al. 2023). However, after monitoring AT 2019avd for over 1500 days in optical, there is no sign of a second rebrightening (i.e., a third flare), as seen in partial TDEs. In fact, the optical evolution of AT 2019avd is more similar to that of a TDE with successive rebrightening events (see the examples in Figure 9 of Yao et al. 2023), although AT 2019avd is the only TDE candidate for which the rebrightening is stronger than the initial one. In conclusion, the properties of AT 2019avd do not resemble those seen in on-axis jetted TDEs or partial TDEs.

In AT 2019avd, the rapid dimming is followed by a soft-to-hard state transition and the spectrum continuously hardens. At the same time, the radio emission in phase 5 seems to increase. Similar phenomena have been observed in the microquasar GRS 1915105. Motta et al. (2021) report a strong radio flare accompanied by a significant reduction in X-ray activity and a hardening of the spectrum. In addition, a local absorber is required to describe the spectrum shape, so they attributed the reduction in X-ray flux to the high inhomogeneous absorption. Different from GRS 1915 + 105, the column density in AT 2019avd has remained at the Galactic value, and thus in our case the decrease in luminosity should be intrinsic and be related to accretion activity.

Rapid changes in luminosity from stellar-mass to SMBHs have been attributed to radiation pressure instability, as one of the explanations, e.g., for the BHXRBs GRS 1915 + 105 (Belloni et al. 2000; Neilsen et al. 2012) and IGR J17091–3624 (Altamirano et al. 2011; Wang et al. 2018), the intermediate BH HLX–1 (Wu et al. 2016), and the AGN IC 3599 (Grupe et al. 2015). Wu et al. 2016 further suggest that this type of variability may exist in different accreting BHs on timescales proportional to the BH mass. Following the empirical relationship between the bolometric luminosity and the variability duration of different types of BHs provided by Wu et al. (2016), the timescale of the corresponding variability of AT 2019avd with a mass of $\sim 10^{6.3}\,M_{\odot}$ should be a couple of years. Although we missed the rising phase of the X-ray flare, the duration of the main flare (i.e., from phases 0–4, roughly 400 days) is marginally consistent with the above relationship. However, we monitored AT 2019avd for another year after phase 4, but did not observe rebrightening from optical to X-rays, despite the sparse data, which conflicts with the scenario of recurrent flares caused by radiation pressure instability.

In jetted TDEs, Zauderer et al. (2013) argue that the rapid decline in X-rays of Swift 1644 + 57 corresponds to the closure of the relativistic jet, which is most likely a consequence of the decrease in the mass accretion rate below the critical value. Regarding AT 2019avd, although there are only four radio detections spanning roughly 3 yr, Wang et al. (2023) were able to fit the multi-epoch radio SED with the self-absorbed synchrotron model developed by Granot & Sari (2002), and the result suggests that the radio flux increases by 50% during the flaring episode (from Day –106 to 348). The latest VLASS detection of AT 2019avd on Day 846 reveals a further increase in flux density at 3 GHz to 2.8 mJy. This is roughly six times higher than the prediction of the synchrotron model, suggesting that the radio flare is either still in the rising phase or has reached its peak in phase 5 and is now declining. Although the uncertainties on the radio-band behavior of the source are large, the combination of several facts (the sub-Eddington state transition, the consequent X-ray spectral hardening, the high radio brightness of $\sim 5 \times 10^6$ K, the optically thick radio emission at low frequencies, and the variable radio luminosity of the source) reconciles with the interpretation of an accretion–ejection coupling similar to what is observed in BHXRBs (Fender et al. 2004) and low-luminosity jetted AGN (Ho 2008; Heckman & Best 2014; Baldi et al. 2021), powered by an advection-dominated accretion flow (ADAF; e.g., Narayan & Yi 1994; Esin et al. 1997; Falcke et al. 2004). These are evidence that jet-related activities could secondarily contribute to the X-ray emission in AT 2019avd.

If the inner region of the accretion disk evaporates into a thick ADAF as the mass accretion rate decreases, this could result in a gradually hardening X-ray spectrum. To interpret the fast formation of the accretion disk in AT 2019avd, Wang et al. (2023) propose a slim disk with a large height-to-radius ratio to reduce the viscous timescale. If the late-time X-ray emission in AT 2019avd could be attributed to an inefficiently radiated ADAF due to a decrease in the mass accretion rate, a slim disk to ADAF evolution is required. Moreover, as indicated by Wang et al. (2023), distinguishing between a thermal or nonthermal source for the late-time X-ray emission (Days 373–615) poses a statistical challenge. Nevertheless, it is worth noting that both the temperature and photospheric radius obtained from the `bbody` model are notably smaller than those observed during the rest time. This unphysical combination suggests that the X-ray emission may likely have departed from its thermal origin, coinciding with the VLBA detection. A BHXRB could be transformed from a very high luminous state to a hard dim state in less than 300 days, while the mass accretion rate decreases by several orders of magnitude (see Figure 12 of Esin et al. 1997). This timescale is in line with what we observed in AT 2019avd. Theoretical work is required to examine the slim disk to ADAF transition scenario.

### 4.4. State Transition

Sub-Eddington systems (e.g., BHXRBs and CLAGN) undergo state transitions, either from hard to soft or vice versa. Especially, the soft-to-hard transitions always occur at a few percent of Eddington luminosity, independent of the mass of the accretor (Maccarone 2003; Done et al. 2007; Noda & Done 2018). At the same time, state transitions have also been observed in super-Eddington systems, such as ULXs (Sutton et al. 2013; Middleton et al. 2015a; Gúrpide et al. 2021), related to changes in mass-transfer rates and the subsequent narrowing of the opening angle of the supercritical funnel, which has been proposed to play a decisive role in their spectral state (e.g., Middleton et al. 2015a; Gúrpide et al. 2021).

As discussed above, AT 2019avd has shown some similarities with BHXRBs. However, its high variability and ultrasoft spectrum make it different from canonical BHXRBs, but more consistent with ULXs. Especially, its spectrum in phases 1–3 is akin to that of the supersoft ultraluminous state in ULXs (see Figure 2 in Kaaret et al. 2017). For instance, we found that AT 2019avd shares certain resemblances with the supersoft ULX NGC 247 (e.g., Feng et al. 2016; Alston et al. 2021; D'Aì et al. 2021). Both sources display a spectrum primarily dominated by a blackbody, accompanied by extreme variability. Moreover, the blackbody temperature of the NGC 247 ULX also remains roughly constant, while its luminosity changes by a factor of ∼6 (see Table 3 of D'Aì et al. 2021). However, as AT 2019avd evolved to phases 4 and 5, its spectrum turned out to be a power-law-like spectrum, which has not been observed in supersoft ULXs. Although based on the adopted mass of $10^{6.3}\,M_{\odot}$ (Malyali et al. 2021), the X-ray luminosities of AT 2019avd do not exceed the super-Eddington luminosity, and the mass is estimated via an empirical mass estimation technique, which carries large systematic uncertainties. We therefore do not exclude the possibility that AT 2019avd first exhibited super-Eddington accretion properties in phases 1–3, when $L_{\rm X} > 0.01\,L_{\rm Edd}$, and then switched to a sub-Eddington accretion regime in phases 4–5, when $L_{\rm X} \leqslant 0.01\,L_{\rm Edd}$, as proposed by Wang et al. (2023).

AT 2019avd has also exhibited several other characteristics that set it apart from BHXRBs, AGN, and ULXs. First, there is almost no hard X-ray emission above 2 keV during the flare, which has been a common feature of TDEs. Besides, comparable spectral hardening behavior has been observed in some X-ray TDEs, e.g., NGC 5905 (Bade et al. 1996), RX J1242–1119 (Komossa et al. 2004), and AT2018fyk (Wevers et al. 2021), and it has been argued to be evidence for the formation of a corona. Wang et al. (2023) reported that the late-time VLBA detection of AT 2019avd could be due to the formation of a compact jet. As hard X-rays can also be produced by relativistic particles via synchrotron radiation, it is unclear whether the spectrum hardening of AT 2019avd is due to the formation of a corona, the launching of jets, ADAF, or a combination of several causes. Second, the softer-when-brighter relationship in AT 2019avd is scaled with but not limited by the Eddington luminosity. Unlike some BHXRBs and AGN, where this trend becomes invalid or even opposite when $L_{\rm X} > 0.02\,L_{\rm Edd}$ (e.g., Kubota & Makishima 2004; Sobolewska et al. 2011), such a relationship in AT 2019avd holds instead for luminosities of 0.007–0.24 $L_{\rm Edd}$ (see Figure 4). Finally, the photon index of AT 2019avd is very steep. Even after the source went into a `powerlaw`-dominated state, the photon index, $\Gamma$=3.1–4.9 in phase 4 and $\Gamma$=1.9–2.7 in phase 5, is still steeper than the one measured in similar states of BHXRBs and AGN, but again consistent with a TDE scenario. We plan to continually monitor this target and see whether it will eventually evolve to the standard hard state and how long it will take to draw a full evolution of the accretion process.

## 5. Conclusion

AT 2019avd has exhibited high X-ray variability on both short (hundreds to thousands of seconds) and long (years) timescales. Together with its spectral features, it has shown some common and unique properties:

1. A rapid drop in X-rays occurs ∼225 days after the peak of the flare, followed by a soft-to-hard transition when the luminosity decreases down to 0.01 $L_{\rm Edd}$, by the possible ejection of an optically thick radio outflow (Wang et al. 2023);
2. The softer-when-brighter relation has been observed throughout the flare: the spectrum hardens as the luminosity decreases;
3. The fractional rms amplitude is high, with an average of 43%, and its evolution is related to the spectral state—the variability may be attributed to some clumpy outflows intercepting the X-ray emission from the accretion disk; and
4. A soft excess has been detected at least in the relatively soft state, whose temperature remains more or less constant while the luminosity decreases by over 1 order of magnitude—none of the standard accretion disk models nor optically thick Comptonization nor the reflection of the disk emission could explain its origin.

## Acknowledgments

The authors thank the anonymous referee for the constructive comments. The authors thank Erlin Qiao, Ian McHardy, Chris Done, Weimin Yuan, Lian Tao, and Rongfeng Shen for the discussion. Y.W. acknowledges support from the Strategic Priority Research Program of the Chinese Academy of Sciences (grant No. XDB0550200) and the Royal Society Newton Fund. L.J. acknowledges the National Natural Science Foundation of China (grant No. 12173103). R.D.B. acknowledges the support from PRIN INAF 1.05.01.88.06 "Toward the SKA and CTA era: discovery, localization, and physics of transient sources."

## Data Availability

Swift, NICER, Chandra. This paper employs a list of Chandra data sets, obtained by the Chandra X-ray Observatory, contained in DOI:10.25574/cdc.170.

## Appendix A
## Estimation of the Contamination Level in the NICER FOV

According to the record from SIMBAD, besides AT 2019avd, there were another three targets—1RXS J082334.6 + 042030, 2MASX J08232985 + 0423327, and IC 505—in the NICER FOV when pointing at the location of AT 2019avd. We show the stacked images of all the XRT observations in the left panel of Figure A1, with a total

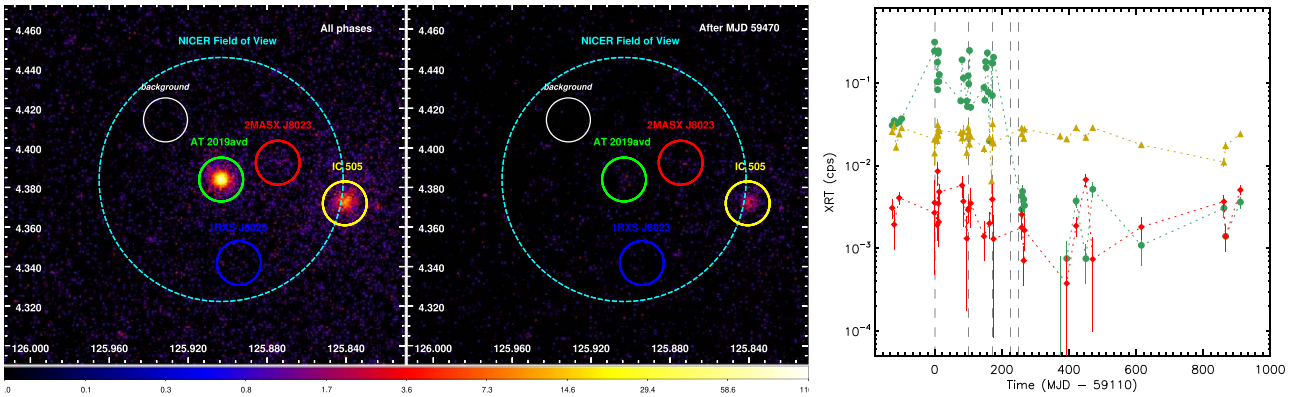


**Figure A1.** Left: stacked images of the XRT data from all the phases and after MJD 59470, respectively. The solid and dashed circular radii are 40″ and 3.′7, respectively. The coordinates of each target are adopted from SIMBAD. Right: XRT lightcurves of AT 2019avd (green), IC 505 (yellow), and 2MASX J0823 (red), calculated in 0.3–2 keV.

**Table 1**
The Best-fitting Parameters for the Spectra of IC 505, 2MASX J0823, and AT 2019avd

| Model | IC 505 EPIC-pn[a] | IC 505 XRT | IC 505 XTI | 2MASX J0823 XRT | AT 2019avd XRT | AT 2019avd XTI |
|---|---|---|---|---|---|---|
| $N_{\rm H}(10^{20}\ {\rm cm}^{-2})$ | 2.4[b] | 2.4[b] | 2.4[b] | 2.4[b] | 2.4[b] | 2.4[b] |
| $\Gamma$ | $1.6\pm0.1$ | $1.3\pm0.4$ | $1.6\pm0.1$ | $0.9^{+1.0}_{-0.5}$ | $2.5\pm0.4$ | $1.7\pm0.1$ |
| $F(10^{-12}\ {\rm erg\ cm^{-2}\ s^{-1}})$ | $0.32\pm0.02$ | $0.25\pm0.05$ | $1.38\pm0.04$ | $0.08\pm0.02$ | $0.13\pm0.03$ | $0.89\pm0.05$ |
| $E_{\rm gau}$ (keV) | $0.93\pm0.01$ | $0.93\pm0.02$ | $0.96\pm0.01$ | ⋯ | 1.03[c] | $1.03\pm0.03$ |
| eqw (keV) | $1.41\pm0.17$ | $0.15\pm0.03$ | $0.52\pm0.04$ | ⋯ | 0.28[c] | $0.28\pm0.07$ |
| $F_{\rm gau}(10^{-12}\ {\rm erg\ cm^{-2}\ s^{-1}})$ | $0.28\pm0.02$ | $0.25\pm0.04$ | $0.43\pm0.02$ | ⋯ | <0.02 | $0.14\pm0.03$ |
| $F_{\rm tot}(10^{-12}\ {\rm erg\ cm^{-2}\ s^{-1}})$ | $0.61\pm0.02$ | $0.50\pm0.03$ | $1.80\pm0.03$ | $0.08\pm0.02$ | $0.13\pm0.03$ | $1.03\pm0.04$ |
| $\chi^2/\nu$ | 21.91/24 | 84.55/117 | 106.98/85 | 11.76/12 | 10.82/13 | 29.68/20 |
| MJD | 57120 | 58982–60020 | 59965–59996 | 59470–60020 | 59470–60020 | 59965 |

**Notes.**
[a] The EPIC-pn spectrum was downloaded directly from the 4XMM-DR12 catalog: http://xmm-catalog.irap.omp.eu/.
[b] The extinction is fixed at its Galactic value, obtained from the HI4PI Collaboration et al. (2016).
[c] The GAUSSIAN centroid energy and equivalent width are fixed at the best-fitting parameters obtained from the fit to the NICER spectrum.

exposure of ∼66 ks. The four targets are marked with a solid circle with a radius of 40″ in Figure A1, with a comparison of the NICER FOV with a radius of 3.′7. As the brightness of 1RXS J082334.6 + 042030 (hereafter 1RXS J0823) is consistent with the background emission, we excluded it from the following analysis. 2MASX J08232985 + 0423327 (hereafter 2MASX J0823) has been defined as an AGN, which has been marginally detected by XRT. The third target, IC 505, has been classified as a LINER AGN, with an emission line centered around 1 keV. We show the lightcurves of the three X-ray sources with XRT data in the right panel of Figure A1 and their best-fitting parameters inferred from different instruments in Table 1. Both the lightcurve and the spectral parameters of IC 505 suggest that it is a rather stable target. AT 2019avd used to be the brightest one among the four targets when it was in the flaring episode; it evolved to be fainter than IC 505 following phase 5, with its flux becoming comparable to 2MASX J0823 after MJD 59470. The fluxes of AT 2019avd and IC 505 detected by XTI are higher than those detected by XRT, indicating that the NICER detections have been contaminated to some extent. We aim to study the NICER data from phases 1–4, when 2MASX J0823 was still fainter than AT 2019avd. Hence, the contamination from 2MASX J0823 should be negligible.

In the next step, we carefully examined the contamination level from IC 505 in the NICER observations of AT 2019avd. As shown in Table 1, there are no targets other than IC 505 presenting significant emission lines around 1 keV, which had already been observed in the XMM-Newton spectrum of IC 505 in 2015. We jointly fitted the most recent NICER data of AT 2019avd and IC 505 and found that the line flux in the former spectrum is roughly 40% of that in the latter spectrum. We then defined a model, i.e., `const*tbabs*zashift (powerlaw+gaussian)`, with the best-fitting parameters to the IC 505 XTI spectrum (see Table 1) and `const`=0.4, as a template for the contamination. Finally, we loaded the template as part of the AT 2019avd data and fitted the left residuals as the net emission from AT 2019avd.

To justify the spectral hardening of AT 2019avd shown in the NICER data, we have also calculated the hardness ratio of IC 505 and the background of AT 2019avd with the XRT and the XTI data, respectively, and plotted the results in Figure A2. The figures show that the spectrum of IC 505 softened over the course of the flare of AT 2019avd. On the other hand, while the hardness of the AT 2019avd background remained roughly constant in phases 1–3 and decreased in phase 4, the background-included spectrum of AT 2019avd hardened monotonically. This fact indicates that the spectral hardening of AT 2019avd is more significant than the softening of its

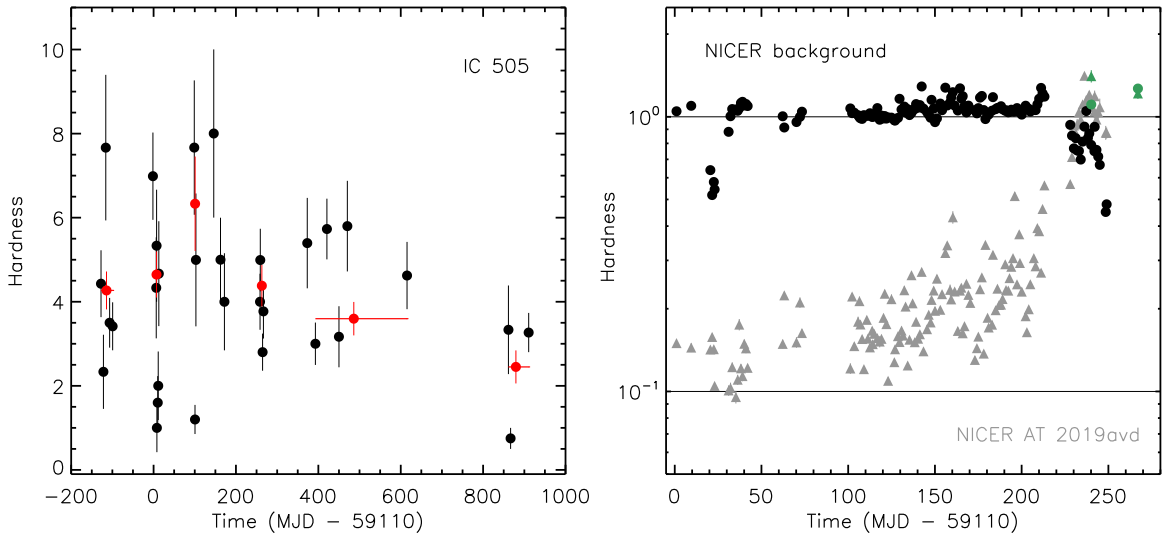


**Figure A2.** Left: the hardness ratio of the XRT data of IC 505. The red dots represent the average of the hardness ratio over different periods. The periods are defined in the same way as in Figure 1. Right: the hardness ratios of the NICER data (background included; gray/green triangles) and the background (black/green dots) of AT 2019avd, respectively. The green dots indicate the hardness ratio measured with the NICER data taken on Days 855 and 882, respectively.

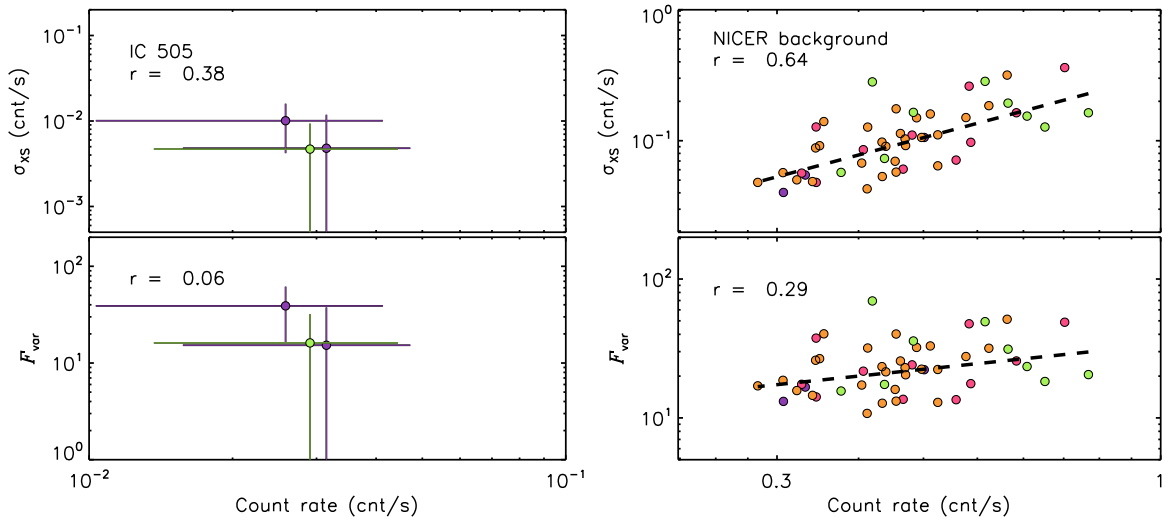


**Figure A3.** Absolute and fractional rms vs. count rate. The upper and lower panels correspond to the XRT data of IC 505 and the NICER background of AT 2019avd. $r$ represents the linear Pearson correlation coefficient. The colors are defined in the same way as in Figure 3.

background. All these results support the spectral hardening detected by AT 2019avd with the NICER data not being an artifact.

## Appendix B
## Measurement of Fractional rms Variability Amplitude

We computed the fractional rms variability amplitude, $F_{\rm var}$, as described in Vaughan et al. (2003), as follows. The observed variance, $S$, can be measured from the lightcurve directly as

$$S^2 = \frac{1}{N-1}\sum_{i=1}^{N}(x_i - \overline{x})^2, \tag{B1}$$

where $\overline{x}$ is the mean of the time series $x_i$ ($i = 0, 1, 2,..,N$). Generally, $x_i$ should be evenly sampled. In the case of AT 2019avd, the variability is on timescales longer than several hundred of seconds, corresponding to the length of one GTI. Therefore, we defined $x_i$ as the average count rate of one GTI and chose observations with two constraints—$N \geqslant 4$ and the observation time between $x_0$ and $x_N$ is longer than 10 ks—to reduce the bias in the results caused by the observation cadences.

As a lightcurve $x_i$ should have finite uncertainties $\sigma_{{\rm err},i}$, due to measurement errors (e.g., Poisson noise), the intrinsic source variance would correspond to the "excess variance," which is the variance after subtracting the contribution expected from the measurement errors:

$$\sigma_{\rm XS}^2 = S^2 - \overline{\sigma_{\rm err}^2}, \tag{B2}$$

where $\overline{\sigma_{\rm err}^2}$ is the mean square error:

$$\overline{\sigma_{\rm err}^2} = \frac{1}{N}\sum_{i=1}^{N}\sigma_{{\rm err},i}^2. \tag{B3}$$

Here, $\sigma_{\rm XS}$ is the absolute rms. $F_{\rm var}$ is the square root of the normalized excess variance:

$$F_{\rm var} = \sqrt{\frac{S^2 - \overline{\sigma_{\rm err}^2}}{\bar{x}^2}}. \quad \text{(B4)}$$

Finally, the uncertainty on $F_{\rm var}$ is given by

$$\mathrm{err}(F_{\rm var}) = \sqrt{\left(\frac{1}{2N}\frac{\overline{\sigma_{\rm err}^2}}{\bar{x}^2 F_{\rm var}}\right)^2 + \left(\frac{\overline{\sigma_{\rm err}^2}}{N}\frac{1}{\bar{x}}\right)^2}. \quad \text{(B5)}$$

We have also calculated the $\sigma_{XS}$ and $F_{\rm var}$ of IC 505 and the AT 2019avd background with the XRT and XTI data and their Pearson correlation. Unfortunately, there are only a few XRT data for IC 505 fulfilling the criteria for the computation of $F_{\rm var}$, and the most significant detection is $F_{\rm var} = 0.39 \pm 0.23$. Regarding the background, its absolute rms amplitude is strongly correlated to the count rate ($r > 0.5$); the fractional rms amplitude is also correlated to the count rate, but the dependence reduces ($r < 0.3$). Overall, the high variability of AT 2019avd detected by NICER should be entirely intrinsic.

## Appendix C
## Temporal Evolution of the Spectral Parameters

We illustrate the evolution of the spectral parameters along with the flare in Figure C2. As shown in the first panel, the column density ranges among $(0.24–0.86) \times 10^{21}$ cm$^{-2}$, and in some observations it pegs at the lower limit, which is the value of the Galactic X-ray absorption in the direction of AT 2019avd (HI4PI Collaboration et al. 2016). We also see from the figure that while the `bbody` flux changes over 1 order of magnitude from phase 1 to phase 3 (the fourth panel), the `bbody` temperature remains more or less constant, although it is accompanied by some scatter (the second panel). The `bbody` temperatures obtained by fitting the XRT spectra are added to the same panel of Figure C2 as magenta dots, which are in good agreement with the NICER data. The photon index ranges between 1.22 and 6.23 and tends to disperse. When the flux significantly drops in phase 4 (the fifth panel), $\Gamma$ is on average lower than the other phases, indicating the hardening of the spectrum.

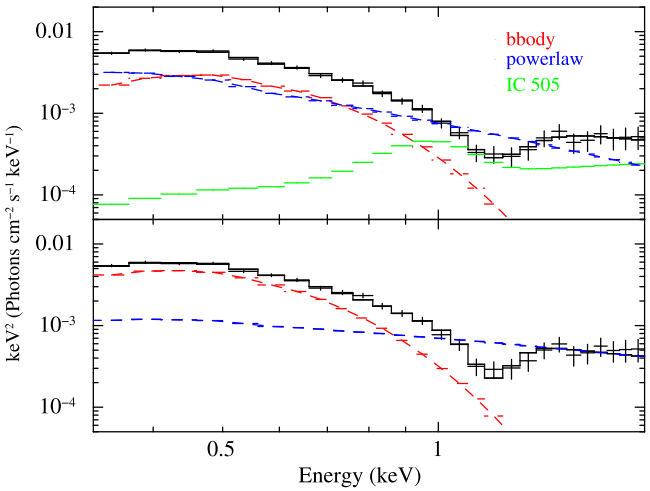


**Figure C1.** Unfolded spectra of ObsID. 3201770178 from phase 2 with (upper) and without (lower) the subtraction of the IC 505 template.

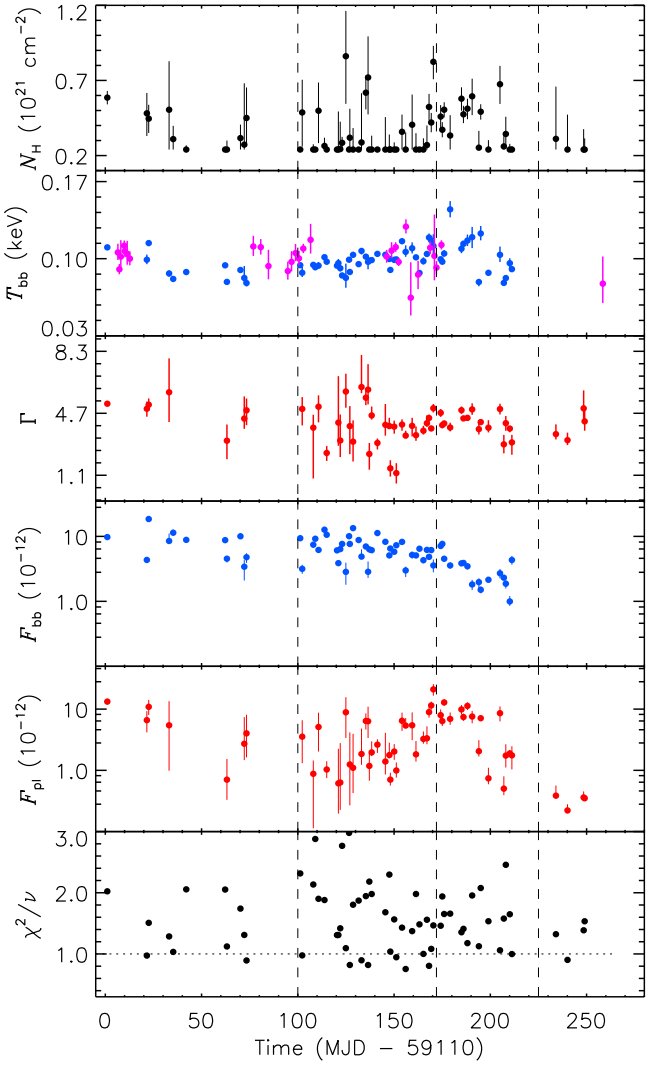


**Figure C2.** Evolution of the spectral parameters. From top to bottom, the column density, the blackbody temperature, the photon index, the `bbody` flux, the `powerlaw` flux, and the reduced $\chi^2$. The magenta dots represent the values of $T_{\rm bb}$ inferred from the XRT spectrum.

## Appendix D
## Determination of the PSDs and Search for Periodicity

To search for any periodicity of the NICER data, we conducted an analysis of the PSDs of the NICER long-term lightcurve in units of GTI. Briefly, the method we used is an adaption of the original method proposed by Done et al. (1992) and improved by Uttley et al. (2002), which relies on simulating lightcurves with a given PSD and imprinting the same sampling pattern as the observed one, in order to reverse engineer the process that generated the observed lightcurve. The lightcurves were simulated using the method of Emmanoulopoulos et al. (2013), initially with a binning equal to half of the minimum exposure time of the NICER GTI and 20 times longer than the observed lightcurve, to introduce aliasing and red-noise leakage effects. For the PSD, we chose a `powerlaw` model ($S \propto f^{-}\beta$) characteristic of accreting sources (Vaughan et al. 2003), whereas for the probability density function we fitted the observed count rates using two log normal distributions. Because in practice we are simulating a long lightcurve and snipping it into segments of the desired length, we additionally added a break at $0.5/T$ to the PSD, following

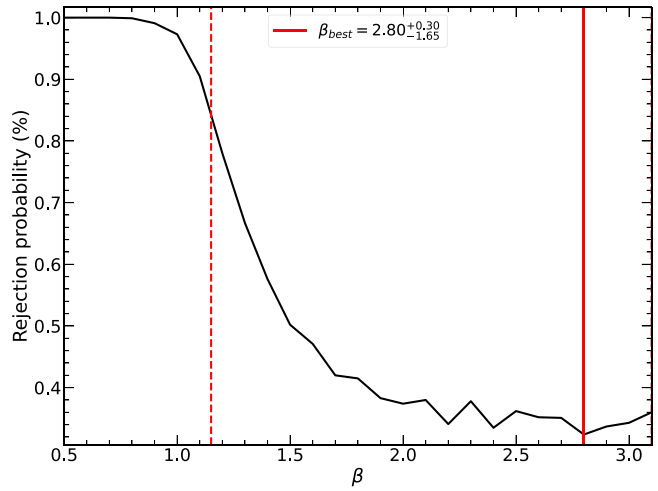


**Figure D1.** Rejection probability contour for the index of the power-law PSD model ($S \propto f^{-}\beta$). The best-fit value is indicated by the solid line and the approximate uncertainties (see the text for details) by the dashed line.

Middleton & Done (2010), after which the PSD breaks to a flat power law.

We generated 2000 lightcurves for each trial $\beta$ value, ranging from 0.5 to 3.2 in steps of 0.1, added Poisson noise, based on the lightcurve exposure times, and compared the Lomb–Scargle periodogram of the observed data with that of the simulations using the statistic proposed by Uttley et al. (2002). We determined the rejection probabilities, following their work, and determined the uncertainties by adding $1\sigma$ to the rejection probability found for the best-fit value, following Markowitz (2010). We are aware that determining the uncertainties using the method of Uttley et al. (2002) is a subtle issue that likely requires additional Monte Carlo simulations (see the discussion in Markowitz 2010), but in order to limit the computational burden we assume the simplistic approach introduced by Markowitz (2010). We also note that considering the uncertainties as defined by Uttley et al. (2002), we obtain very similar results (see below).

We evaluated the periodogram from $1/2 <dt>$, where $<dt>$ is the median sampling time (a replacement for the nonexistent Nyquist frequency; VanderPlas 2018), to $1/T$, where $T$ is the baseline of the GTIs, using a frequency spacing equal to $N \times 1/T$, where $N$ is the oversampling factor, which we set to 2 (which we justify below). The periodograms were rebinned logarithmically following Papadakis & Lawrence (1993)—so fewer samples are required to reach Gaussianity—to have at least 20 powers per bin. We note that while the powers in the Lomb–Scargle periodogram are known *not* to be independent—violating the assumption of independent samples inherent in the $\chi^2$ statistic—we found this problem is mitigated as long as the periodogram is rebinned and not too oversampled. We verified this through Monte Carlo simulations of lightcurves with known PSDs, and found that with a logarithmic rebinning of ∼15–20 powers per bin and an oversample factor of 1–2, the recovered $\beta$ value had a bias of 0.1 or less when using the $\chi^2$ statistic. The resulting contours for $\beta$ are shown in Figure D1. This simple model cannot be statistically rejected, and a rather wide range of $\beta$ values would be compatible with the data (rejection probability <60%). Approximately, our best-fit $\beta$ value is found to be $\beta = 2.8^{+0.3}_{-1.65}$. Considering the uncertainties as defined by Uttley et al. (2002) would reduce the lower limit only slightly, to ∼1.3.

We next used the best-fit model (together with its uncertainties) as the null hypothesis to test for the presence of any periodicity in the periodogram. We retrieved 5000 lightcurves, taking into account the uncertainties on $\beta$ (so as to take the uncertainties into account for the false-alarm probability derivation; Vaughan 2005), and looked for the highest peak in the corresponding periodograms of each generated lightcurve. The results are shown in Figure 5, which show the $3\sigma$ one-trial (green line) and multiple-trial (dashed line) false-alarm probabilities. We see that there is no obvious peak above the false-alarm probability levels. The highest peak at around 25 days is well below the one-trial false-alarm probability. We thus conclude that the variability of AT 2019avd is fully consistent with the typical aperiodic variability commonly observed across all accreting systems.

## ORCID iDs

Yanan Wang https://orcid.org/0000-0003-3207-5237
Diego Altamirano https://orcid.org/0000-0002-3422-0074
Matthew Middleton https://orcid.org/0000-0002-8183-2970
Santiago del Palacio https://orcid.org/0000-0002-5761-2417
Muryel Guolo https://orcid.org/0000-0002-5063-0751
Poshak Gandhi https://orcid.org/0000-0003-3105-2615
Shuang-Nan Zhang https://orcid.org/0000-0001-5586-1017
Ronald Remillard https://orcid.org/0000-0003-4815-0481
Dacheng Lin https://orcid.org/0000-0001-5683-5339
Megan Masterson https://orcid.org/0000-0003-4127-0739
Ranieri D. Baldi https://orcid.org/0000-0002-1824-0411
Jon M. Miller https://orcid.org/0000-0003-2869-7682
Andrea Sanna https://orcid.org/0000-0002-0118-2649

## References

Alabarta, K., Méndez, M., García, F., et al. 2022, MNRAS, 514, 2839
Alexander, K. D., van Velzen, S., Horesh, A., & Zauderer, B. A. 2020, SSRv, 216, 81
Alston, W. N., Pinto, C., Barret, D., et al. 2021, MNRAS, 505, 3722
Altamirano, D., Belloni, T., Linares, M., et al. 2011, ApJL, 742, L17
Altamirano, D., & Strohmayer, T. 2012, ApJL, 754, L23
Atapin, K., Fabrika, S., & Caballero-García, M. D. 2019, MNRAS, 486, 2766
Auchettl, K., Guillochon, J., & Ramirez-Ruiz, E. 2017, ApJ, 838, 149
Bade, N., Komossa, S., & Dahlem, M. 1996, A&A, 309, L35
Baldi, R. D., Williams, D. R. A., Beswick, R. J., et al. 2021, MNRAS, 508, 2019
Ballantyne, D. R., Ross, R. R., & Fabian, A. C. 2001, MNRAS, 327, 10
Bellm, E. C., Kulkarni, S. R., Graham, M. J., et al. 2019, PASP, 131, 018002
Belloni, T., Homan, J., Casella, P., et al. 2005, A&A, 440, 207
Belloni, T., Klein-Wolt, M., Méndez, M., van der Klis, M., & van Paradijs, J. 2000, A&A, 355, 271
Blagorodnova, N., Neill, J. D., Walters, R., et al. 2018, PASP, 130, 035003
Brown, J. S., Holoien, T. W. S., Auchettl, K., et al. 2017, MNRAS, 466, 4904
Chen, J.-H., Dou, L.-M., & Shen, R.-F. 2022, ApJ, 928, 63
D'Aì, A., Pinto, C., Del Santo, M., et al. 2021, MNRAS, 507, 5567
Done, C., Gierliński, M., & Kubota, A. 2007, A&ARv, 15, 1
Done, C., Madejski, G. M., Mushotzky, R. F., et al. 1992, ApJ, 400, 138
Emmanoulopoulos, D., McHardy, I. M., & Papadakis, I. E. 2013, MNRAS, 433, 907
Esin, A. A., McClintock, J. E., & Narayan, R. 1997, ApJ, 489, 865
Falcke, H., Körding, E., & Markoff, S. 2004, A&A, 414, 895
Fender, R., & Belloni, T. 2004, ARA&A, 42, 317
Fender, R. P., Belloni, T. M., & Gallo, E. 2004, MNRAS, 355, 1105
Feng, H., Tao, L., Kaaret, P., & Grisé, F. 2016, ApJ, 831, 117
Gezari, S. 2021, ARA&A, 59, 21
Gezari, S., Chornock, R., Rest, A., et al. 2012, Natur, 485, 217
Gierliński, M., & Done, C. 2004, MNRAS, 349, L7
Gleissner, T., Wilms, J., Pottschmidt, K., et al. 2004, A&A, 414, 1091
Granot, J., & Sari, R. 2002, ApJ, 568, 820

Grupe, D., Komossa, S., & Saxton, R. 2015, ApJL, 803, L28
Gúrpide, A., Godet, O., Vasilopoulos, G., Webb, N. A., & Olive, J. F. 2021, A&A, 654, A10
Hammerstein, E., van Velzen, S., Gezari, S., et al. 2023, ApJ, 942, 9
Heckman, T. M., & Best, P. N. 2014, ARA&A, 52, 589
Heil, L. M., & Vaughan, S. 2010, MNRAS, 405, L86
Heil, L. M., Vaughan, S., & Uttley, P. 2012, MNRAS, 422, 2620
HI4PI Collaboration, Ben Bekhti, N., Flöer, L., et al. 2016, A&A, 594, A116
Hills, J. G. 1975, Natur, 254, 295
Hinkle, J. T., Holoien, T. W. S., Shappee, B. J., et al. 2020, ApJL, 894, L10
Hjellming, R. M., Rupen, M. P., Mioduszewski, A. J., et al. 1999, ApJ, 514, 383
Ho, L. C. 2008, ARA&A, 46, 475
Holoien, T. W. S., Auchettl, K., Tucker, M. A., et al. 2020, ApJ, 898, 161
Holoien, T. W. S., Kochanek, C. S., Prieto, J. L., et al. 2016, MNRAS, 455, 2918
Homan, J., Klein-Wolt, M., Rossi, S., et al. 2003, ApJ, 586, 1262
Jiang, Y.-F., Stone, J. M., & Davis, S. W. 2014, ApJ, 796, 106
Jin, C., Done, C., & Ward, M. 2021, MNRAS, 500, 2475
Kaaret, P., Feng, H., & Roberts, T. P. 2017, ARA&A, 55, 303
Kaastra, J. S., & Bleeker, J. A. M. 2016, A&A, 587, A151
Kallman, T., & Bautista, M. 2001, ApJS, 133, 221
Kara, E., Alston, W. N., Fabian, A. C., et al. 2016, MNRAS, 462, 511
Kara, E., Dai, L., Reynolds, C. S., & Kallman, T. 2018, MNRAS, 474, 3593
King, A., & Pounds, K. 2015, ARA&A, 53, 115
Komossa, S., & Bade, N. 1999, A&A, 343, 775
Komossa, S., Halpern, J., Schartel, N., et al. 2004, ApJL, 603, L17
Kubota, A., & Makishima, K. 2004, ApJ, 601, 428
Leahy, D. A., Darbro, W., Elsner, R. F., et al. 1983, ApJ, 266, 160
Lin, D., Maksym, P. W., Irwin, J. A., et al. 2015, ApJ, 811, 43
Lipunova, G. V. 1999, AstL, 25, 508
Liu, Z., Malyali, A., Krumpe, M., et al. 2023, A&A, 669, A75
Lyubarskii, Y. E. 1997, MNRAS, 292, 679
Maccarone, T. J. 2003, A&A, 409, 697
Malyali, A., Rau, A., Merloni, A., et al. 2021, A&A, 647, A9
Markowitz, A. 2010, ApJ, 724, 26
Middleton, M., & Done, C. 2010, MNRAS, 403, 9
Middleton, M. J., Heil, L., Pintore, F., Walton, D. J., & Roberts, T. P. 2015a, MNRAS, 447, 3243
Middleton, M. J., Walton, D. J., Fabian, A., et al. 2015b, MNRAS, 454, 3134
Middleton, M. J., Sutton, A. D., & Roberts, T. P. 2011, MNRAS, 417, 464
Miller, J. M., Kaastra, J. S., Miller, M. C., et al. 2015, Natur, 526, 542
Motta, S. E., Kajava, J. J. E., Giustini, M., et al. 2021, MNRAS, 503, 152
Mucciarelli, P., Casella, P., Belloni, T., Zampieri, L., & Ranalli, P. 2006, MNRAS, 365, 1123
Mummery, A. 2021, MNRAS, 507, L24
Muñoz-Darias, T., Motta, S., & Belloni, T. M. 2011, MNRAS, 410, 679
Narayan, R., Saàdowski, A., & Soria, R. 2017, MNRAS, 469, 2997
Narayan, R., & Yi, I. 1994, ApJL, 428, L13
Neilsen, J., Remillard, R. A., & Lee, J. C. 2012, ApJ, 750, 71
Noda, H., & Done, C. 2018, MNRAS, 480, 3898
Papadakis, I. E., & Lawrence, A. 1993, MNRAS, 261, 612
Pasham, D. R., Ho, W. C. G., Alston, W., et al. 2022, NatAs, 6, 249
Pasham, D. R., Lucchini, M., Laskar, T., et al. 2023, NatAs, 7, 88
Pasham, D. R., Remillard, R. A., Fragile, P. C., et al. 2019, Sci, 363, 531
Petrucci, P. O., Ursini, F., De Rosa, A., et al. 2018, A&A, 611, A59
Pinto, C., Middleton, M. J., & Fabian, A. C. 2016, Natur, 533, 64
Rees, M. J. 1984, ARA&A, 22, 471
Reis, R. C., Miller, J. M., Reynolds, M. T., et al. 2012, Sci, 337, 949
Remillard, R. A., Loewenstein, M., Steiner, J. F., et al. 2022, AJ, 163, 130
Remillard, R. A., & McClintock, J. E. 2006, ARA&A, 44, 49
Ross, R. R., & Fabian, A. C. 1993, MNRAS, 261, 74
Sadowski, A., & Narayan, R. 2016, MNRAS, 456, 3929
Saxton, C. J., Soria, R., Wu, K., & Kuin, N. P. M. 2012a, MNRAS, 422, 1625
Saxton, R. D., Read, A. M., Esquej, P., et al. 2012b, A&A, 541, A106
Saxton, R., Komossa, S., Auchettl, K., & Jonker, P. G. 2021, SSRv, 217, 18
Scaringi, S., Körding, E., Uttley, P., et al. 2012, MNRAS, 421, 2854
Shakura, N. I., & Sunyaev, R. A. 1973, A&A, 500, 33
Singh, K. P., Garmire, G. P., & Nousek, J. 1985, ApJ, 297, 633
Sobolewska, M. A., Papadakis, I. E., Done, C., & Malzac, J. 2011, MNRAS, 417, 280
Stiele, H., & Kong, A. K. H. 2017, ApJ, 844, 8
Strohmayer, T. E., & Mushotzky, R. F. 2003, ApJL, 586, L61
Sutton, A. D., Roberts, T. P., & Middleton, M. J. 2013, MNRAS, 435, 1758
Takeuchi, S., Ohsuga, K., & Mineshige, S. 2013, PASJ, 65, 88
Takeuchi, S., Ohsuga, K., & Mineshige, S. 2014, PASJ, 66, 48
Uttley, P., & McHardy, I. M. 2001, MNRAS, 323, L26
Uttley, P., McHardy, I. M., & Papadakis, I. E. 2002, MNRAS, 332, 231
van Velzen, S., Gezari, S., Hammerstein, E., et al. 2021, ApJ, 908, 4
van Velzen, S., Holoien, T. W. S., Onori, F., Hung, T., & Arcavi, I. 2020, SSRv, 216, 124
VanderPlas, J. T. 2018, ApJS, 236, 16
Vaughan, S. 2005, A&A, 431, 391
Vaughan, S., Edelson, R., Warwick, R. S., & Uttley, P. 2003, MNRAS, 345, 1271
Wang, Y., Baldi, R. D., del Palacio, S., et al. 2023, MNRAS, 520, 2417
Wang, Y., Ji, L., Zhang, S. N., et al. 2020, ApJ, 896, 33
Wang, Y., Méndez, M., Altamirano, D., et al. 2018, MNRAS, 478, 4837
Wevers, T., Coughlin, E. R., Pasham, D. R., et al. 2023, ApJL, 942, L33
Wevers, T., Pasham, D. R., van Velzen, S., et al. 2021, ApJ, 912, 151
White, N. E., & Marshall, F. E. 1984, ApJ, 281, 354
Wolff, M. T., Guillot, S., Bogdanov, S., et al. 2021, ApJL, 918, L26
Wu, Q., Czerny, B., Grzedzielski, M., et al. 2016, ApJ, 833, 79
Yao, Y., Lu, W., Guolo, M., et al. 2022, ApJ, 937, 8
Yao, Y., Ravi, V., Gezari, S., et al. 2023, ApJL, 955, L6
Zauderer, B. A., Berger, E., Margutti, R., et al. 2013, ApJ, 767, 152